

## Porous Silicon Gradient Refractive Index Micro-Optics

Neil A. Krueger,<sup>†</sup> Aaron L. Holsteen,<sup>‡</sup> Seung-Kyun Kang,<sup>†</sup> Christian R. Ocier,<sup>†</sup> Weijun Zhou,<sup>§</sup> Glennys Mensing,<sup>||</sup> John A. Rogers,<sup>†</sup> Mark L. Brongersma,<sup>‡</sup> and Paul V. Braun<sup>\*,†</sup>

<sup>†</sup>Department of Materials Science and Engineering, Department of Chemistry, Frederick Seitz Materials Research Laboratory, and Beckman Institute, University of Illinois at Urbana–Champaign, Urbana, Illinois 61801, United States

<sup>‡</sup>Geballe Laboratory for Advanced Materials, Stanford University, Stanford, California 94305, United States

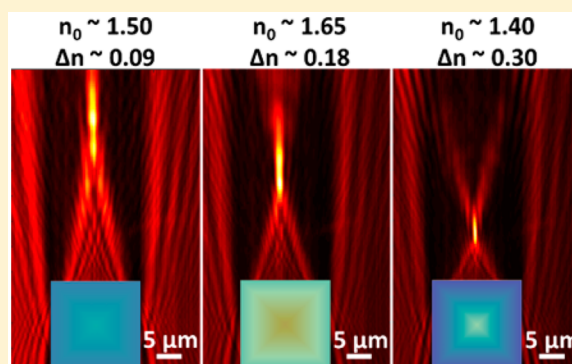
<sup>§</sup>The Dow Chemical Company, 2301 N. Brazosport Boulevard, B-1470, Freeport, Texas 77541, United States

<sup>||</sup>Department of Mechanical Science and Engineering, University of Illinois at Urbana–Champaign, Urbana, Illinois 61801, United States

### Supporting Information

**ABSTRACT:** The emergence and growth of transformation optics over the past decade has revitalized interest in how a gradient refractive index (GRIN) can be used to control light propagation. Two-dimensional demonstrations with lithographically defined silicon (Si) have displayed the power of GRIN optics and also represent a promising opportunity for integrating compact optical elements within Si photonic integrated circuits. Here, we demonstrate the fabrication of three-dimensional Si-based GRIN micro-optics through the shape-defined formation of porous Si (PSi). Conventional microfabrication creates Si square microcolumns (SMCs) that can be electrochemically etched into PSi elements with nanoscale porosity along the shape-defined etching pathway, which imparts the geometry with structural birefringence. Free-space characterization of the transmitted intensity distribution through a homogeneously etched PSi SMC exhibits polarization splitting behavior resembling that of dielectric metasurfaces that require considerably more laborious fabrication. Coupled birefringence/GRIN effects are studied by way of PSi SMCs etched with a linear (increasing from edge to center) GRIN profile. The transmitted intensity distribution shows polarization-selective focusing behavior with one polarization focused to a diffraction-limited spot and the orthogonal polarization focused into two laterally displaced foci. Optical thickness-based analysis readily predicts the experimentally observed phenomena, which strongly match finite-element electromagnetic simulations.

**KEYWORDS:** Microlenses, transformation optics, silicon photonics, birefringence



Gradient refractive index (GRIN) elements possess spatially varying refractive indices, endowing them with the ability to send light along curvilinear optical paths, as Fermat's principle explains, because light travels stationary, extremal trajectories within optically inhomogeneous media.<sup>1</sup> This behavior enables powerful optical elements such as Luneburg lenses, which are devoid of geometrical aberrations and offer high efficiency fiber-to-chip coupling.<sup>2–4</sup> Other designer GRINs are embodied by elements decoupling physical geometry and optical function, such as carpet cloaks<sup>5,6</sup> and flat lenses.<sup>7</sup> Flat lenses, particularly flat, Si-based microlenses, are attractive for compact, on-chip optics within the framework of integrated Si photonics.<sup>7</sup> Additionally, the presence of coupled birefringence/GRIN effects provides an opportunity for a GRIN element to perform distinct, polarization-selective operations.<sup>8</sup> However, to date conventional processing, which lithographically nanostructures bulk Si to define the local refractive index, has confined Si-based GRIN elements to thin, 2D geometries.<sup>2–7</sup> Here, we fabricate 3D birefringent GRIN micro-

optics by electrochemically etching preformed Si microstructures (e.g., square microcolumns) into porous Si (PSi) structures with defined refractive index profiles. These elements perform novel, polarization-dependent optical functions, including splitting and focusing, expanding the use of PSi for a wide range of integrated photonics applications.

Porous silicon (PSi) was initially studied due to its visible luminescence at room temperature<sup>9,10</sup> but has since established an identity as a versatile optical material,<sup>11</sup> as its nanoscale porosity (and thus refractive index) can be modulated during its electrochemical fabrication.<sup>12,13</sup> During fabrication, a time-varying etch current density results in a porosity (and thus refractive index) gradient along the etch pathway. This effect has most notably been used to form 1D optical super-

**Received:** July 15, 2016

**Revised:** October 4, 2016

**Published:** October 31, 2016

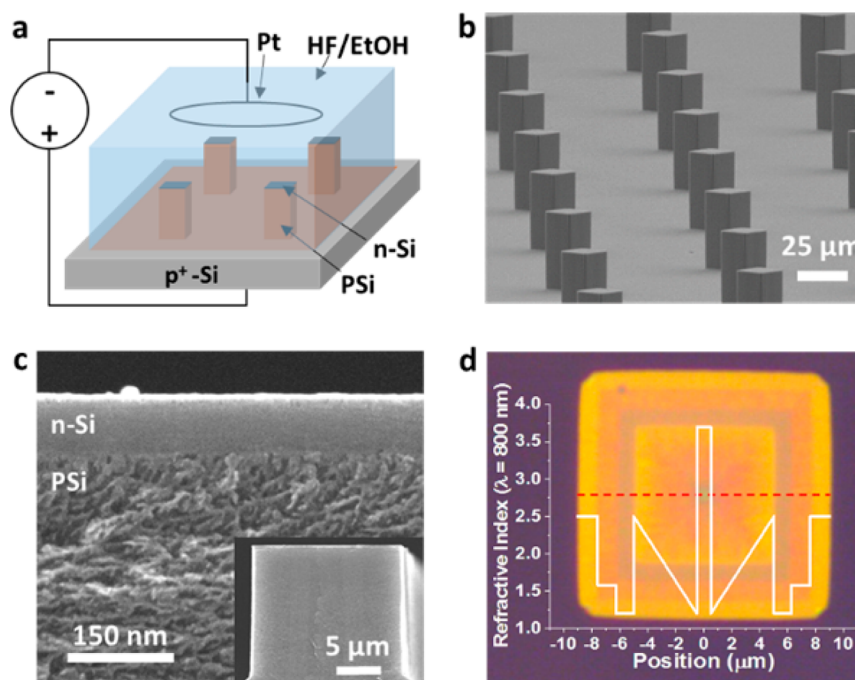


**Figure 1.** Shape-defined electrochemical etching of PSi for GRIN micro-optics. (a) Schematic outlining the process by which p-type Si SMCs with n-type caps undergo shape-defined electrochemical etching to endow them with nanoscale porosity that defines the local refractive index. (b) SEM image of a section of an array of Si SMCs subjected to shape-defined PSi formation. (c) SEM cross-section of an etched feature showing how PSi formation proceeds beneath the n-type cap. (Inset) SEM cross-section of a fully porous ridge, showing that shape-defined etching can proceed through the Si microstructures. (d) Reflection-mode optical micrograph from the top of an  $\sim 18 \mu\text{m}$  PSi SMC with an arbitrary GRIN that can be observed through the structure's n-type Si cap. The GRIN profile along the dashed red line is superimposed on top of the optical image.

lattices<sup>14,15</sup> that can be exploited as chemical sensors.<sup>16–19</sup> Refractive index modulation in 2D or 3D as required for a GRIN element, however, is more difficult in that it requires a spatially varying current density. This can be accomplished by using shaped electrodes<sup>20</sup> but the approach is limited in that the etch rate of PSi also varies with current density,<sup>21,22</sup> making flat elements unattainable. Additionally, current spreading in the substrate and electrolyte prevent sharp GRIN variations like those that can be achieved with a time-varying current density. Photomediated etching offers an attractive route to arbitrary 2D PSi GRIN structures<sup>23</sup> but is restricted to thin (e.g., 2–3  $\mu\text{m}$ ) structures due to optical absorption in the PSi. We suggest that a versatile approach to 3D GRIN elements is to use a defined Si topography to serve as the starting point for the lateral etch required to form a GRIN profile. Now, a time-varying current density generates the GRIN along the PSi etch pathway that initiates at all unmasked Si/electrolyte interfaces (Figure 1a). While nonplanar electrochemical processing has been shown for Si<sup>24,25</sup> and Ge,<sup>26</sup> the previous work only utilized the shape-defined etch pathway to form conventional optical superlattices.

Our process begins with a p<sup>+</sup>-type Si wafer doped to form a shallow ( $\sim 100 \text{ nm}$ ) n-type surface. Photolithography, followed by deep reactive ion etching, generates an array of microscale elements (e.g., square microcolumns (SMCs)) with less than 10 nm roughness sidewalls (Figure S1) across the wafer (Figure 1b). Electrochemical etching (Figure 1a) simultaneously converts all of the elements to PSi in a few minutes. The n-type cap restricts PSi formation<sup>27</sup> to the sidewalls, resulting in an etch path and GRIN profile that runs inward from and perpendicular to each of the SMC sidewalls (Figure 1c). Changes in the current density, whether discrete or continuous, provide nearly arbitrary and highly reproducible control over

the refractive index (Figures S2–S4) and porosity (Figure S5) of PSi.

As a demonstration, an SMC (Figure 1d) is etched with a current density profile consisting of three discrete segments of 20, 200, and 400  $\text{mA cm}^{-2}$ , followed by a linear increase from 20 to 400  $\text{mA cm}^{-2}$ . The resulting GRIN profile (Figure 1d) is visibly manifested by the color appearing from the thin-film interference within the SMC's n-type Si cap. As shown in this demonstration, one can leave a bulk Si core, further extending the accessible refractive index range and providing possibilities for exotic devices coupling GRINs with a functional Si core. As is common for (100) mesoporous PSi, the pores align in domains with their long axis normal to the surface where they initiated, creating for the SMC four domains with aligned pores that converge at the center of the element (Figure 2b). This has interesting optical implications, as PSi possesses a large, positive birefringence ( $n_e - n_o \approx 0.1–0.2$ ) with the optic axis defined by the pore orientation.<sup>28,29</sup> Henceforth, for simplicity, we assume a constant value of  $n_e - n_o = 0.15$ .

Optical characterization of the PSi SMCs is performed by mechanically removing them from the Si substrate and dispersing them on a glass substrate, where most elements end up lying flat on their side (Figure S6). The schematic shown in Figure 2c summarizes the major parameters governing the optical response of the PSi SMCs. TM polarization will see the four domains as having the same refractive index, while TE polarization will interact with the ordinary refractive index ( $n_o$ ) in the top and bottom domains and the (higher) extraordinary refractive index ( $n_e$ ) in the left and right domains. Superimposed on any birefringence effects is the applied GRIN, represented here by a pair of general, truncated polynomials of order  $m$  that vary along the  $z$ -

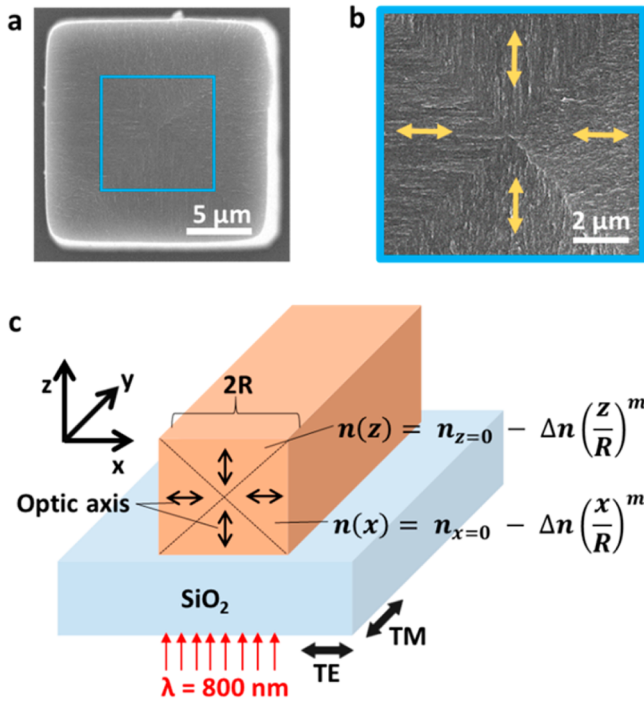


**Figure 2.** Structural and optical analysis of PSi SMCs. (a) Low-magnification SEM image of the base of a fully etched PSi SMC. (b) Higher-magnification SEM image of the boxed region in panel a, which shows the convergence of four domains with defined pore orientation and optic axis, represented by the yellow arrows. (c) Schematic representing the major parameters to consider in the optical performance of PSi SMCs.

direction for the top and bottom domains and along the  $x$ -direction for the left and right domains. As a simple predictor of birefringent and GRIN effects, one can look at the integrated optical thickness (OPT) (i.e., integrated along  $z$ -direction) across the  $x$ -direction of the sample as

$$\text{OPT}(x) = \int n(z)dz + n(x)dz \quad (1)$$

After integrating eq 1 (see Supporting Information for details), it is found that

$$\text{OPT}(x) = \frac{2\Delta n}{R^m} \left( \frac{1}{m+1} - 1 \right) |x|^{m+1} + 2(n_{x=0} - n_{z=0})|x| + 2R \left( n_{z=0} - \frac{\Delta n}{m+1} \right) \quad (2)$$

where  $R$  is one-half of the side length.

For a purely birefringent structure ( $\Delta n = 0$ )

$$\text{OPT}_{\text{TM}}(x) = 2R(n_o) \quad (3)$$

$$\text{OPT}_{\text{TE}}(x) = 2(n_e - n_o)|x| + 2R(n_o) \quad (4)$$

with  $x = 0$  defined to be at the center of the SMC. As expected, the transverse magnetic (TM) OPT is uniform across the structure given the homogeneous refractive index (Figure 3a), indicating that TM light should pass through unperturbed. The transverse electric (TE) response is more complicated in that the positive birefringence and internal structure (i.e., the convergent trajectory of the pores in the four domains) couple such that the OPT increases linearly toward the edge of the SMC (Figure 3b), suggesting that TE light will be diverged by

its interaction with the birefringent SMC. Simulations performed with COMSOL Multiphysics Modeling Software (Figure 3c,d), optical measurements at 800 nm (Figure 3e,f), and OPT-based predictions all strongly agree for both the TM and TE cases. The agreement between simulation and experiment even includes the observed small amount of TM beam convergence, which we speculate to be a result of diffractive effects at the edge of the SMC. Interestingly, these simple structures exhibit functionality comparable to that of dielectric metasurfaces proposed for pixel-integrated polarization splitters.<sup>30</sup> We suggest that birefringent structures generated by shape-defined formation of PSi could offer a powerful option for realizing such elements without the need for processes like electron-beam lithography.

While the birefringence of PSi SMCs results in interesting properties, our primary interest is to exploit PSi's refractive index modulation capabilities. Here, we show that a linear GRIN (i.e.,  $m = 1$ ) generates a parabolic OPT capable of polarization-selective light focusing. Inserting  $m = 1$  into eq 2 yields

$$\text{OPT}_{\text{TM}}(x) = \frac{-\Delta n}{R} |x|^2 + 2R \left( n_{o,z=0} - \frac{\Delta n}{2} \right) \quad (5)$$

$$\text{OPT}_{\text{TE}}(x) = \frac{-\Delta n}{R} |x|^2 + 2(n_{e,x=0} - n_{o,z=0})|x| + 2R \left( n_{o,z=0} - \frac{\Delta n}{2} \right) \quad (6)$$

which are plotted in Figure 4a,b, respectively. TM light focusing by the linear GRIN PSi SMC is readily observed in simulation (Figure 4c), while the TE case is more complex, with an OPT profile consisting of adjacent parabolas (Figure 4b) that are functionally equivalent to two side-by-side lenses. The simulation of the structure's TE behavior (Figure 4d) is characterized by two high-intensity focal regions laterally displaced to either side of the single TM focus. To fabricate this linear GRIN element, we etch an SMC with a current density graded from  $\sim 286$  to  $\sim 163$  mA cm<sup>-2</sup> (Supporting Information) such that the (ordinary) refractive index increases linearly from  $\sim 1.4$  to  $\sim 1.7$  (edge to center). The experimentally measured TM and TE intensity distributions (Figure 4e,f) strongly agree with simulations. Under TM illumination, the measured back focal length is  $\sim 10$   $\mu$ m, which can be modulated by changing the magnitude of the GRIN variation (Figure S13), while the roughly measured convergence (half) angle from the back surface is  $\sim 30^\circ$ , suggesting a numerical aperture of  $\sim 0.5$ . As such, a diffraction-limited focal spot is  $\sim \lambda$  (800 nm in this case), which agrees well with the full-width half-maximum of the intensity trace along the focal plane in Figure 4e. For TE illumination, there is a slight deviation from the simulation results, which may be a result of the value of birefringence that was used and its assumed spatial invariance. Still, our simple assumptions very reasonably capture the coupled birefringent/GRIN response for a linear GRIN PSi SMC.

In summary, we have presented a new technique for fabricating birefringent GRIN micro-optics based on the shape-defined formation of PSi. Using an SMC geometry, we showed that the birefringence of a homogeneous PSi structure offers opportunities beyond dielectric metasurfaces for easily fabricated polarization splitters. Additionally, we demonstrated that a PSi SMC possessing a linear GRIN is capable of focusing

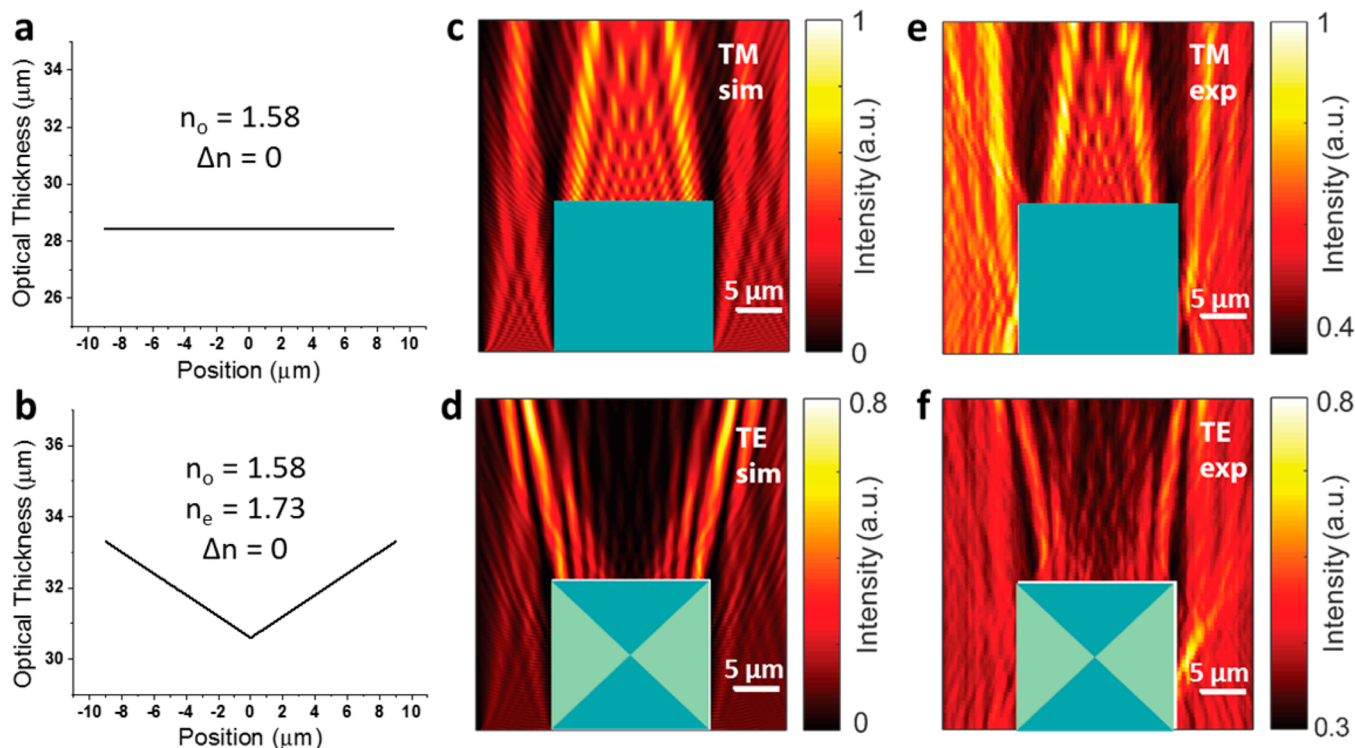


**Figure 3.** Polarization routing with birefringent PSi SMCs. (a) Integrated OPT for TM polarization interacting with a homogeneously etched PSi SMC, which is optically flat. (b) Integrated OPT for TE polarization interacting with a homogeneously etched PSi SMC, which exhibits a linear OPT profile expected to diverge light. (c) Simulated intensity distribution for TM polarization interacting with a homogeneously etched PSi SMC confirming that light passes through largely unperturbed with the exception of a small amount of beam convergence attributed to diffraction effects at the edges of the PSi SMC. (d) Simulated intensity distribution for TE polarization interacting with a homogeneously etched PSi SMC confirming that light should diverge as a result of the birefringence and internal structure. (e,f) Experimental intensity distributions for TM and TE polarizations, respectively, that are in strong agreement with simulations. (c,d) Panels are normalized to the maximum intensity observed in simulation, whereas (e,f) are normalized to the maximum intensity observed in experiment.

TM light to a diffraction-limited line, while TE light is directed to two high-intensity regions in roughly the same plane as, but laterally displaced to either side of, the TM focus. The optical physics of these structures is readily predictable, while the flexibility of the fabrication process lends itself to scaling to dimensions on the order of 100–200 μm if appropriate measures are taken to promote uniformity (e.g., electrolyte stirring<sup>31</sup> and etching breaks<sup>32</sup>) of the electrochemical etch. In light of these results, we envision possibilities beyond polarization-selective pixels, such as tailoring geometries (Supporting Information) and GRIN profiles for on-chip optical “Janus” devices<sup>33</sup> capable of performing modal operations like conversion or splitting as part of photonic integrated circuits.

**Methods. Silicon Microcolumn Fabrication.** Fabrication was performed on 4 in. diameter, highly doped ( $\rho \sim 0.001$ – $0.005 \Omega \text{ cm}$ ) p-type (100) Si wafers (Topsil). Wafers were cleaned with Nanostrip for 10 min at 70 °C, followed by deposition of  $\sim 1.5 \mu\text{m}$  of  $\text{SiO}_2$  by plasma-enhanced chemical vapor deposition on the backside to serve as a diffusion barrier. N-type doping was performed for  $\sim 10$  min at 1000 °C in a furnace containing a solid-state phosphorus source. After doping, the wafer was cleaned again with Nanostrip, followed by removal of all  $\text{SiO}_2$  by immersing in 48% hydrofluoric acid (aq) for 2 min at room temperature. Photolithography was performed by processing SPR220-4.5 (Shipley) positive photoresist under manufacturer recommended conditions and exposing with an EVG620 mask aligner (EV Group).

Development with AZ MIF 917 (AZ Electronic Materials) reveals arrays of photoresist squares with their sides oriented such that the resulting Si square microcolumn sidewalls will align with (100) degenerate crystal planes (which allows PSi etching calibration to be performed with flat pieces of (100) Si). Si etching was performed with a Pegasus ICP-DRIE (SPTS Technologies) running a Bosch process. After a final cleaning with Nanostrip, the Si wafer is cleaved into  $\sim 15 \text{ mm} \times 15 \text{ mm}$  square chips containing a  $\sim 3 \text{ mm} \times 3 \text{ mm}$  array of square microcolumns and placed in an electrochemical cell for PSi etching.

**Porous Silicon Etching.** Etching was carried out in a polypropylene cell with an exposed etch area of  $\sim 1.20 \text{ cm}^2$ . The electrolyte comprised a 1:1 volume ratio of 48% hydrofluoric acid (aq) and 100% ethanol. A 5 mm diameter Pt–Ir inoculating loop (Thomas Scientific) served as the counter electrode. Contact to the back of the SMC-containing Si chip was established with a stainless steel electrode. Current was delivered to the cell by an SP-200 research grade potentiostat/galvanostat (Bio-Logic Science Instruments). The current waveforms for generating GRIN samples were constructed via BenchLink Waveform Builder Pro software (Keysight Technologies, Inc.) and sent to the SP-200 through a 33220A Function/Arbitrary Waveform Generator (Keysight Technologies, Inc.). After etching, all samples were thoroughly rinsed with ethanol and dried under a gentle stream of nitrogen.

**Optical Characterization.** PSi refractive index versus wavelength information at specific fabrication current densities

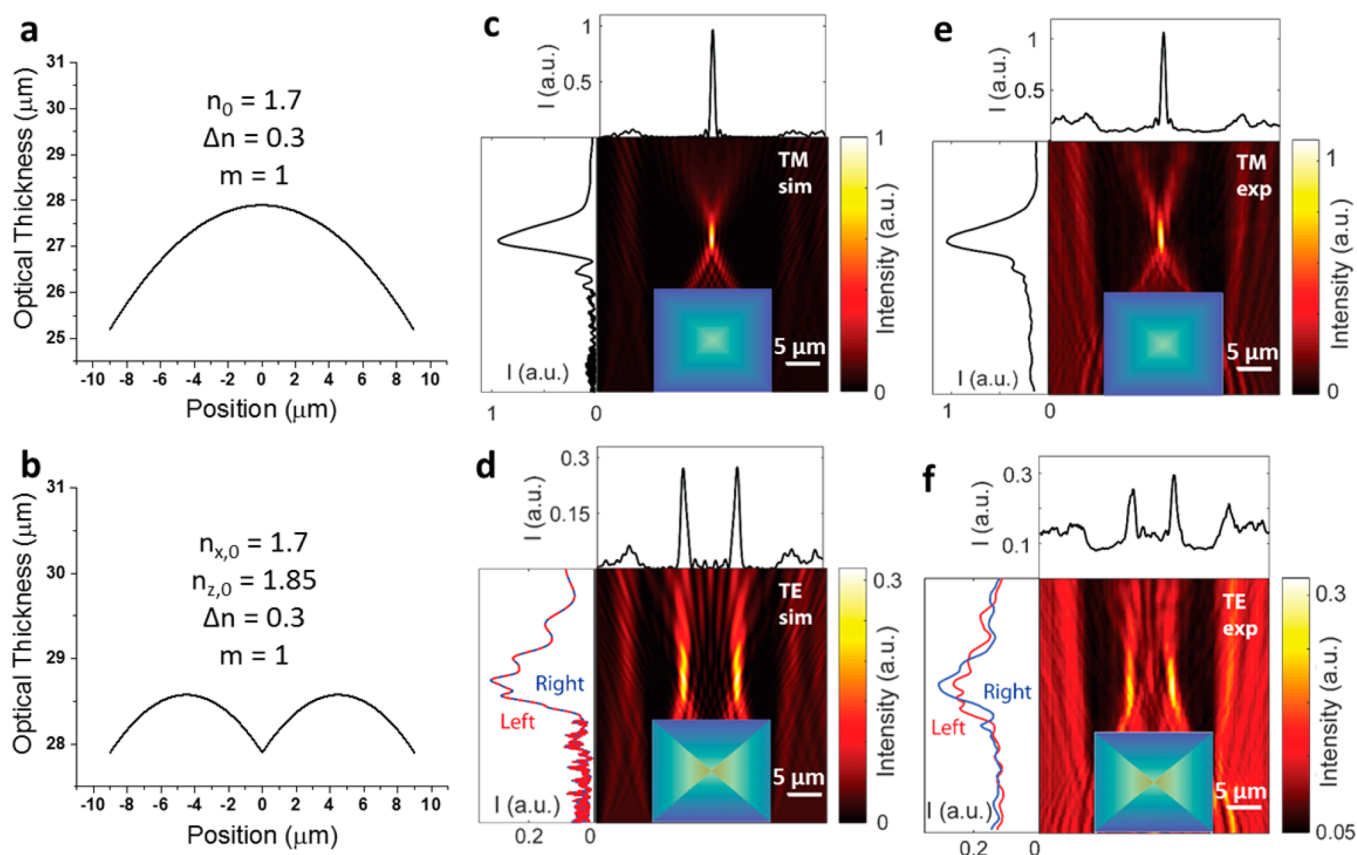


**Figure 4.** Light focusing with linear GRIN PSi SMCs. (a) Integrated OPT for TM polarization interacting with a linear GRIN PSi SMC that possesses a lens-like radius of curvature. (b) Integrated OPT for TE polarization interacting with a linear GRIN PSi SMC that exhibits two adjacent regions possessing a radius of curvature, which is functionally equivalent to two side-by-side lenses. (c) Simulated intensity distribution for TM polarization interacting with a linear GRIN PSi SMC, as expected, focusing is observed. (d) Simulated intensity distribution for TE polarization interacting with a linear GRIN PSi SMC that exhibits two high-intensity regions laterally displaced from the simulated TM focus. (e,f) Experimental intensity distributions for TM and TE polarizations, respectively, that are in strong agreement with simulations. (c,d) Panels are normalized to the maximum intensity observed in simulation, while (e,f) are normalized to the maximum intensity observed in experiment. In (c–f), the top and side panels represent traces that are transverse to and along the propagation direction, respectively, and run through the region(s) of maximum intensity.

was extracted from the reflectance spectrum of planar thin films (Figure S2). Reflectance spectra were collected using a Si PDA spectrometer (Control Development, Inc.) hooked up to an Axio Observer D1 inverted microscope (Carl Zeiss, Inc.) with a white-light halogen lamp serving as the source. The intensity distribution of the light transmitted through the a PSi SMC was measured using a confocal microscope (Nikon Eclipse, C1) with the optical setup shown in Figure S12. The illumination source was a white light supercontinuum source that is wavelength-tunable from 400 to 2200 nm (NKT, SuperK Extreme). A linear polarizer and a half waveplate are utilized to generate a linearly polarized illumination beam. A substrate with PSi SMCs is mounted on a XYZ scan stage, such that SMC-containing side faces upward toward the microscope objective, and is illuminated from below with the laser beam set to 800 nm. The light intensity in the  $x$ – $y$  plane above the GRIN element (Figure S14) is gathered using a 100 $\times$  objective with a numerical aperture of 0.9 and captured by a high-resolution CCD camera (Princeton Instruments, PIXIS 1024B). By stepping the stage in 500 nm increments, images in the  $x$ – $y$  plane can be stacked in the  $z$ -dimension to construct the light intensity volume above the PSi SMC.

## ■ ASSOCIATED CONTENT

### Supporting Information

The Supporting Information is available free of charge on the ACS Publications website at DOI: 10.1021/acs.nanolett.6b02939.

Additional optical characterization calculations and data (PDF)

## ■ AUTHOR INFORMATION

### Corresponding Author

\*E-mail: pbraun@illinois.edu.

### Author Contributions

N.A.K. and P.V.B. conceived the idea. N.A.K., S.-K.K., W.Z., G.M., J.A.R., and P.V.B. designed and performed the fabrication process. N.A.K., A.L.H., C.R.O., M.L.B., and P.V.B. performed optical characterization, analyzed data, and constructed figures. N.A.K. and P.V.B. wrote the manuscript. All authors commented on the manuscript.

### Notes

The authors declare no competing financial interest.

## ACKNOWLEDGMENTS

This work was supported by the Dow Chemical Company and the U.S. Department of Energy "Light-Material Interactions in Energy Conversion" Energy Frontier Research Center under grant DE-SC0001293. This research was also conducted with Government support under and awarded by DoD, Air Force Office of Scientific Research, National Defense Science and Engineering Graduate (NDSEG) Fellowship, 32 CFR 168a (N.A.K. and A.H.). This research was carried out in part in the Materials Research Laboratory Center for Microanalysis of Materials, the Microscopy Suite and Visualization Laboratory at the Beckman Institute, the Micro and Nanotechnology Laboratory, and the Micro-Nano-Mechanical Systems Cleanroom at the University of Illinois. The authors acknowledge Thomas R. O'Brien, Dr. Hailong Ning, Dr. Hao Chen, and Dr. Julio Soares for insightful discussions regarding optical simulation and characterization.

## REFERENCES

- (1) Leonhardt, U.; Philbin, T. G. In *Progress in Optics*; Wolf, E., Ed.; Elsevier: Amsterdam, 2009; Vol. 53, pp 69–152.
- (2) Di Falco, A.; Kehr, S. C.; Leonhardt, U. *Opt. Express* **2011**, *19* (6), 5156–5162.
- (3) Gabrielli, L. H.; Lipson, M. *Opt. Express* **2011**, *19* (21), 20122–20127.
- (4) Hunt, J.; Tyler, T.; Dhar, S.; Tsai, Y.-J.; Bowen, P.; Larouche, S.; Jokerst, N. M.; Smith, D. R. *Opt. Express* **2012**, *20* (2), 1706.
- (5) Valentine, J.; Li, J.; Zentgraf, T.; Bartal, G.; Zhang, X. *Nat. Mater.* **2009**, *8* (7), 568–571.
- (6) Gabrielli, L. H.; Cardenas, J.; Poitras, C. B.; Lipson, M. *Nat. Photonics* **2009**, *3* (8), 461–463.
- (7) Spadoti, D. H.; Gabrielli, L. H.; Poitras, C. B.; Lipson, M. *Opt. Express* **2010**, *18* (3), 3181–3186.
- (8) Danner, A. J.; Tyc, T.; Leonhardt, U. *Nat. Photonics* **2011**, *5* (6), 357–359.
- (9) Canham, L. T. *Appl. Phys. Lett.* **1990**, *57* (10), 1046–1048.
- (10) Lehmann, V.; Gösele, U. *Appl. Phys. Lett.* **1991**, *58* (8), 856–858.
- (11) Gal, M.; Reece, P. J.; Zheng, W.; Lerondel, G. *Proc. SPIE* **2003**, *5277*, 9–16.
- (12) Smith, R. L.; Collins, S. D. *J. Appl. Phys.* **1992**, *71* (8), R1–R22.
- (13) Zhang, X. G. *J. Electrochem. Soc.* **2004**, *151* (1), C69–C80.
- (14) Frohnhoff, S.; Berger, M. G. *Adv. Mater.* **1994**, *6* (12), 963–965.
- (15) Vincent, G. *Appl. Phys. Lett.* **1994**, *64* (18), 2367–2369.
- (16) Lin, V. S.-Y.; Moteshare, K.; Dancil, K.-P. S.; Sailor, M. J.; Ghadiri, M. R. *Science* **1997**, *278* (5339), 840–843.
- (17) Mulloni, V.; Pavesi, L. *Appl. Phys. Lett.* **2000**, *76* (18), 2523–2525.
- (18) Rong, G.; Najmaie, A.; Sipe, J. E.; Weiss, S. M. *Biosens. Bioelectron.* **2008**, *23* (10), 1572–1576.
- (19) Link, J. R.; Sailor, M. J. *Proc. Natl. Acad. Sci. U. S. A.* **2003**, *100* (19), 10607–10610.
- (20) Ilyas, S.; Gal, M. *Appl. Phys. Lett.* **2006**, *89* (21), 211123–211123–3.
- (21) Collins, B. E.; Dancil, K.-P. S.; Abbi, G.; Sailor, M. J. *Adv. Funct. Mater.* **2002**, *12* (3), 187–191.
- (22) Li, Y. Y.; Kim, P.; Sailor, M. J. *Phys. Status Solidi A* **2005**, *202* (8), 1616–1618.
- (23) Barth, D. S.; Gladden, C.; Salandrino, A.; O'Brien, K.; Ye, Z.; Mrejen, M.; Wang, Y.; Zhang, X. *Adv. Mater.* **2015**, *27* (40), 6131–6136.
- (24) Ruminski, A. M.; Barillaro, G.; Secret, E.; Huang, W. D.; Potocny, A.; Carion, U.; Wertans, C.; Sailor, M. J. *Adv. Opt. Mater.* **2013**, *1* (7), 510–516.
- (25) Mangaiyarkarasi, D.; Breese, M. B. H.; Ow, Y. S. *Appl. Phys. Lett.* **2008**, *93* (22), 221905.
- (26) Kempa, T. J.; Bediako, D. K.; Kim, S.-K.; Park, H.-G.; Nocera, D. G. *Proc. Natl. Acad. Sci. U. S. A.* **2015**, *112* (17), 5309–5313.
- (27) Imai, K. *Solid-State Electron.* **1981**, *24* (2), 159–164.
- (28) Kashkarov, P. K.; Golovan, L. A.; Fedotov, A. B.; Efimova, A. I.; Kuznetsova, L. P.; Timoshenko, V. Y.; Sidorov-Biryukov, D. A.; Zheltikov, A. M.; Haus, J. W. *J. Opt. Soc. Am. B* **2002**, *19* (9), 2273.
- (29) Ishikura, N.; Fujii, M.; Nishida, K.; Hayashi, S.; Diener, J. *Opt. Express* **2008**, *16* (20), 15531.
- (30) Khorasaninejad, M.; Zhu, W.; Crozier, K. B. *Optica* **2015**, *2* (4), 376.
- (31) Ghulinyan, M.; Oton, C. J.; Bonetti, G.; Gaburro, Z.; Pavesi, L. *J. Appl. Phys.* **2003**, *93* (12), 9724–9729.
- (32) James, T. D.; Keating, A. J.; Parish, G.; Musca, C. A. *J. Electrochem. Soc.* **2009**, *156* (9), H744–H750.
- (33) Zentgraf, T.; Valentine, J.; Tapia, N.; Li, J.; Zhang, X. *Adv. Mater.* **2010**, *22* (23), 2561–2564.